Philosophical Magazine
Publication details, including instructions for authors and subscription information:
http://www.tandfonline.com/loi/tphm20

Influence of impurity elements on the nucleation and growth of Si in high purity melt-spun Al-Si-based alloys

J.H. Li [a], M.Z. Zarif [a], G. Dehm [b c] & P. Schumacher [a d]

[a] Chair of Casting Research, Department of Metallurgy, University of Leoben, Franz-Josef Str. 18, A8700 Leoben, Austria

[b] Department of Materials Physics, University of Leoben, Jahnstr. 12, A8700 Leoben, Austria

[c] Erich Schmid Institute of Materials Science, Austrian Academy of Sciences, Jahnstr. 12, A8700 Leoben, Austria

[d] Austrian Foundry Research Institute, Park Str. 18, A8700 Leoben, Austria

Version of record first published: 18 May 2012.

To cite this article: J.H. Li , M.Z. Zarif , G. Dehm & P. Schumacher (2012): Influence of impurity elements on the nucleation and growth of Si in high purity melt-spun Al-Si-based alloys, Philosophical Magazine, 92:31, 3789-3805

To link to this article: http://dx.doi.org/10.1080/14786435.2012.687840

Philosophical Magazine
Vol. 92, No. 31, 1 November 2012, 3789–3805

Taylor & Francis
Taylor & Francis Group

Influence of impurity elements on the nucleation and growth of Si in high purity melt-spun Al–Si-based alloys

J.H. Li[a]*, M.Z. Zarif[a], G. Dehm[bc] and P. Schumacher[ad]

[a]*Chair of Casting Research, Department of Metallurgy, University of Leoben, Franz-Josef Str. 18, A8700 Leoben, Austria;* [b]*Department of Materials Physics, University of Leoben, Jahnstr. 12, A8700 Leoben, Austria;* [c]*Erich Schmid Institute of Materials Science, Austrian Academy of Sciences, Jahnstr. 12, A8700 Leoben, Austria;* [d]*Austrian Foundry Research Institute, Park Str. 18, A8700 Leoben, Austria*

(*Received 23 September 2011; final version received 18 April 2012*)

The nucleation and growth of Si has been investigated by TEM in a series of high purity melt spun Al–5Si (wt%)-based alloys with a trace addition of Fe and Sr. In the as-melt-spun condition, some twinned Si particles were found to form directly from the liquid along the grain boundary. The addition of Sr into Al–5Si-based alloys promotes the twinning of Si particles on the grain boundary and the formation of Si precipitates in the α-Al matrix. The majority of plate-shaped and truncated pyramid-shaped Si precipitates were also found to nucleate and grow along $\{111\}_{\alpha\text{-Al}}$ planes from supersaturated solid solution in the α-Al matrix. In contrast, controlled slow cooling decreased the amount of Si precipitates, while the size of the Si precipitates increased. The orientation relationship between these Si precipitates and the α-Al matrix still remained cube to cube. The β-Al_5FeSi intermetallic was also observed, depending on subsequent controlled cooling.

Keywords: Al–Si alloy; precipitation; TEM; melt spinning; impurity effect

1. Introduction

The precipitation behaviour of Al–Si-based alloy produced by conventional casting has been widely investigated. However, during conventional casting, i.e. direct chill casting, gravity casting, etc., a coarse platelet eutectic silicon that give rise to inferior mechanical properties was observed. Although some success in modifying the eutectic silicon has been achieved by the addition of modifiers and refining agents during the conventional casting process and subsequent heat treatment [1–4], considerable attention has been paid to rapid solidification, i.e. melt spinning [5–12], with the aim of controlling the morphology and distribution of the eutectic silicon, and to further improve the mechanical properties in hypoeutectic Al–Si alloys.

Melt spinning of Al–Si-based alloys leads to fine Si particles formed directly from the liquid during solidification. The precipitation of Si from supersaturated solid solution in the α-Al matrix during subsequent cooling was also greatly enhanced

*Corresponding author. Email: jie-hua.li@hotmail.com

ISSN 1478–6435 print/ISSN 1478–6443 online

http://dx.doi.org/10.1080/14786435.2012.687840
http://www.tandfonline.com

in melt spun Al–Si-based alloys. The finer microstructure and the enhanced hardening effects produce better mechanical properties. The hardness values of the melt-spun ribbons have been reported to be about three times higher than those of ingot counterparts [5–9]. The improvement in mechanical properties of the melt-spun ribbon can be attributed to the supersaturated solid solution and structural refinement. However, the hardness values decreased greatly during ageing at higher temperatures [13]. The decrease in properties after thermal ageing can be attributed to Si precipitation and the subsequent growth or ripening of the Si precipitates [10–12]. A better understanding on the nucleation and growth of Si in melt spun Al–Si-based alloy is of importance to control the morphology of Si precipitates and further improve their thermal stability.

Ternary additions have a great effect on the precipitation of Si in Al–Si-based alloys [13–16]. The addition of Fe often leads to the formation of a variety of stable and metastable intermetallic phases, depending upon alloy composition and the solidification rate above the Al–Si eutectic temperature [1]. These Fe-containing phases may influence the nucleation sequence to form Si in Al–Si–Fe alloys [4]. Research on high purity Al–Si–Fe alloy is of great interest to elucidate the impurity effect of Fe on the nucleation and growth of Si, as suggested by Dahle et al. [4].

The addition of other impurity elements, which segregate to the edges of the growing Si crystals, results in the well-known impurity-induced twinning (IIT) growth mechanism [17] and twin plane re-entrant edge growth mechanism (TPRE) [18,19]. These mechanisms also explain the modification by the addition of Sr and other elements (Yb, Ca, Y, La, K and Na), which show an atomic ratio of $X/Si \approx 1.646$ into Al–Si alloys produced by conventional casting [1–3,14,15]. The element Sr was found to segregate exclusively to the eutectic Si phase in an Al–10Si–1 Cu (wt%) alloy with 250 ppm addition of Sr [14], an Al–15Si alloy with 62 ppm addition of Sr [15] and a commercial hypoeutectic Al–Si foundry alloy (A356) modified with up to 200 ppm Sr [16]. However, to date, there is a lack of the experimental evidence of Sr segregation along the Si twin re-entrant edge in Al–Si-based alloy, although the theoretical prediction was established by Hellawell in the late 1980s [17]. The low Sr concentrations used and the interplay between Si twins and Sr solute atoms at the re-entrant edge of Si precipitates make this observation very challenging. Thus, the effect of Sr within the Si twin remains to be explored.

Here, we report some TEM investigations on the microstructure of high purity melt-spun Al–Si-based alloy with a trace addition of Fe and/or Sr. The aim is to elucidate the precipitation of Si in supersaturated solid solution and to elucidate the effect of Sr and Fe addition on Si twinning during solidification.

2. Experimental methods

A series of high purity Al–5 wt% Si alloys (wt%, used through the paper, in case not specified otherwise) with a trace addition of Fe and Sr were prepared by using arc melting and subsequent melt spinning. As described elsewhere [20], high purity materials (5N Al, 5N Si, 3N8 Fe, 2N Sr) were used to produce Al–5Si (Alloy A), Al–5Si–200 ppm Fe (Alloy B) and Al–5Si–50 ppm Fe–100 ppm Sr (Alloy C). The chemical compositions were given in Table 1. It is noteworthy that the Sr contents

Table 1. Chemical composition of Al–Si-based alloys with and without a trace addition of Fe and Sr (wt%).

Alloy no.	Si	Fe	Sr	Al
Alloy A	5.00	<0.0005	<0.0005	Balance
Alloy B	5.00	0.02	<0.0005	Balance
Alloy C	5.00	0.005	0.01	Balance

(100 ppm in Alloy C) were added with a Al–3.59Sr master alloy manufactured by a 5N Al and 2N Sr.

The ribbons were investigated in the as-melt-spun condition and after heating to 600°C and subsequent continuous cooling in the range from 600 to 400°C with a rate of 10°C/min in a power compensated DSC (Perkin-Elmer Diamond), with the aim to investigate microstructure evolution with respect to thermal history. The thermal response during cooling is the subject of this paper. The ribbons for TEM investigation were mechanically ground, polished and dimpled to about 30 μm, and then ion-beam milled using a Gatan Precision Ion Polishing System (PIPS, Gatan model 691). A constant preparation temperature (about −10°C) was maintained using a cold stage during ion beam polishing. Transmission electron microscopy (TEM) was performed using a Philips CM12 microscopy operated at 120 kV equipped with a CCD camera (GATAN Model 794 MSC BioScan) and an image-side Cs-corrected JEOL-2100F operated at 200 kV.

3. Results

3.1. *As melt spun condition*

3.1.1. *Nucleation and growth of Si particles from the liquid*

Figure 1 shows a Si particle in high purity melt-spun Al–5Si alloy. Si particles were tilted to the principal twinning orientation of Si (⟨110⟩) to perform a twin density measurement. Viewed from the $[011]_{\alpha\text{-Al}}$ zone axis, the Si particle appears twinned, as shown in Figure 1a. However, the twin boundaries were not imaged end-on, leading to a triangular shape in the 2-dimensional projection due to decreasing sample thickness towards the edge (see Figure 1a, white triangle). These twins become invisible when the sample was tilted into the $[001]_{\alpha\text{-Al}}$ zone axis, as shown in Figure 1c. The twin density (i.e. number of twins per length) can be evaluated by counting the number of the twins intersecting a perpendicular reference line (see white line in Figure 1a). An analysis of at least 10 twinned Si particles yields an average twin density of about $1.6 \pm 0.4 \times 10^{-4}\,\mathrm{nm}^{-1}$. For clarity and accuracy, all the measured data is presented with an error bar (standard deviation).

Often, Si particles were found at the grain boundaries, although some twinned Si particles were also rarely observed in the matrix, as shown in Figure 1. We believe that these Si particles form directly from the liquid due to their large size. It should be noted that the Si particles formed directly from the liquid, as described here, are different from the Si precipitates formed from supersaturated solid solution

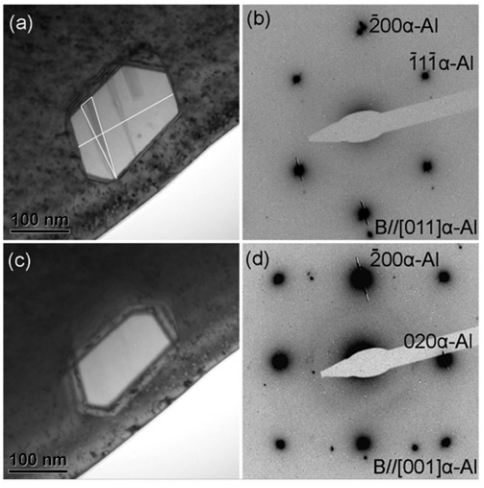

Figure 1. (a, c) TEM bright-field images of a Si particle; (b, d) corresponding $[011]_{\alpha\text{-Al}}$ and $[001]_{\alpha\text{-Al}}$ SADPs in melt-spun Al–5Si (wt%) alloy.

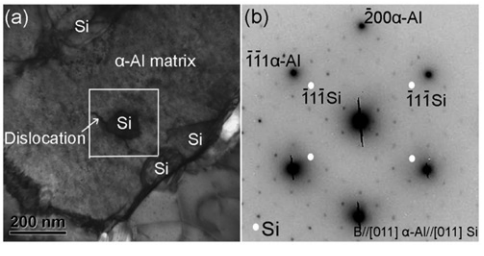

Figure 2. (a) TEM bright-field image of the Si particles, and (b) corresponding $[011]_{\alpha\text{-Al}}$ SADP taken from the area as marked with a white box in (a), in melt-spun Al–5Si–200 ppm Fe (wt%) alloy. The white points represent the diffraction patterns of Si. The un-indexed diffraction points can be attributed to double diffraction.

in the α-Al matrix, as described in Section 3.1.2. It should be also noted that the streaks in the selected area diffraction patterns (SADPs) (Figure 1b and d) are artefacts from the long exposure time of the digital camera used. No other precipitates are present in the α-Al matrix, although some dislocation loops and extended dislocation threading all the way through the foil were observed. This indicates that Si was mainly dissolved in the α-Al matrix owing to the higher cooling rate during melt spinning.

The addition of Fe (up to 200 ppm) into the Al–5Si alloy has no great effect on the as-melt-spun microstructure, i.e. grain size, the size and morphology of Si particles, etc. No Fe-containing phases were observed in the α-Al matrix. Twinned Si particles were again observed in the microstructure. Figure 2 shows a typical microstructure of the high purity melt-spun Al–5Si–200 ppm Fe alloy. Si particles were observed along the grain boundary, and also in the α-Al matrix. The Si particle

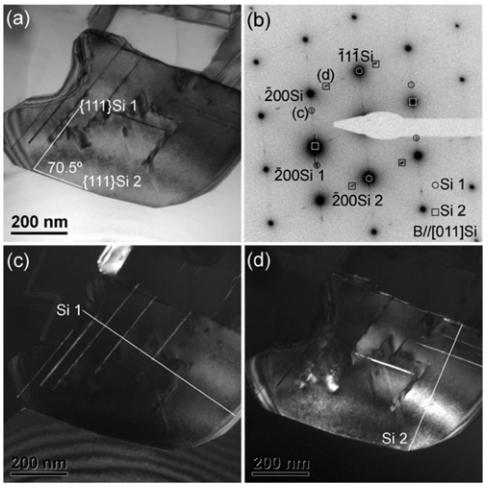

Figure 3. (a) TEM bright-field image, (b) corresponding $[011]_{\alpha\text{-Al}}$ SADP and (c, d) dark-field images using the diffraction spots as marked in (b), taken from melt-spun Al–5Si–50 ppm Fe–100 ppm Sr (wt%) alloy.

in the α-Al matrix appears to interact with some dislocations. More careful observations reveal that most of the rounded Si particles were found in the vicinity of the grain boundaries. The corresponding SADP of a Si particle in the α-Al matrix is shown in Figure 2b. The SADP indicates that Si particles maintain a perfect cube to cube relationship with the α-Al matrix, i.e. $\{111\}_{Si}\langle 011\rangle_{Si}//\{111\}_{\alpha\text{-Al}}\langle 011\rangle_{\alpha\text{-Al}}$. It should be noted that the un-indexed diffraction points can be attributed to the double diffraction of Si due to the fine size of the Si particles (about 50 nm). The same effect was also observed in SADPs for Si precipitates in an Al–Si–Ge alloy [13]. Double diffraction was also observed in several other diffraction patterns, as shown later.

The addition of Sr into the Al–5Si alloy promotes twinning of the Si particles formed during solidification. Most Si particles were multiply twinned. Figure 3 shows a multiply twinned Si particle formed during solidification in high purity melt-spun Al–5Si–50 ppm Fe–100 ppm Sr alloy. The angle between the two different twinning planes is close to 70.5°. The faceted morphology of the twinned Si particle can be understood in terms of the interface energies between Si and Al (as discussed in Section 4.1). The size of the twinned Si particle is approximately 700 nm. This is about three times larger than that in the Al–5Si alloy without any additions of Fe and Sr, as shown in Figure 1a. However, it should be noted that the Si particle in Figure 3 was observed at the grain boundary, while the Si particle in Figure 1 was observed in the α-Al matrix. Generally, the size of Si particles at the grain boundaries is larger than that in the α-Al matrix, as shown in Figure 2. The corresponding SADP (Figure 3b) and the centred dark-field images (Figure 3c and d), using two different diffraction spots as marked in Figure 3b, indicate again that the Si twin grows along $\{111\}_{Si}$ plane. In contrast to the twins described in Figure 1, the twins presented in Figure 3 were imaged end-on. Similar to Figure 1a, the twin density of

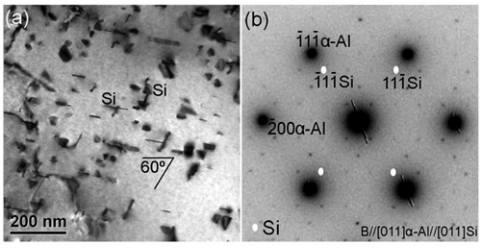

Figure 4. (a) TEM bright-field image, and (b) corresponding $[011]_{\alpha\text{-Al}}$ SADP taken from melt-spun Al–5Si–50 ppm Fe–100 ppm Sr (wt%) alloy. The white points represent the diffraction patterns of Si. The un-indexed diffraction points can be attributed to the double diffraction of Si.

the twins can be also evaluated though counting the number of the twins along the two lines with different directions but perpendicular to the twins, as marked with two white lines in Figure 3c and d, respectively. A total analysis of at least 10 twinned Si particles with two different twinning directions provides a value of $2.7 \pm 1.1 \times 10^{-4}\,\text{nm}^{-1}$ for the average twin density, significantly exceeding the value of $1.6 \pm 0.4 \times 10^{-4}\,\text{nm}^{-1}$ for the high purity Al–5Si alloy. It is very clear that the addition of Sr into Al–5Si alloy promotes twinning of the Si particles formed during solidification.

3.1.2. *Si precipitates in the matrix of high purity melt-spun Al–5Si–50 ppm Fe–100 ppm Sr alloy*

The addition of Sr into the Al–5Si alloy promotes not only the twinning of the Si particles formed during solidification, but also the formation of Si precipitates formed from supersaturated solid solution in the α-Al matrix. Figure 4 shows a typical microstructure in high purity melt-spun Al–5Si–50 ppm Fe–100 ppm Sr alloy. In contrast to the high purity melt-spun Al–5Si alloy and Al–5Si–200 ppm Fe alloy without the addition of Sr, some Si precipitates were observed in the α-Al matrix, as shown in Figure 4a.

Viewed from $\langle 011 \rangle_{\alpha\text{-Al}}$, most of Si precipitates are 100–200 nm in size and plate-like in morphology, as shown in Figure 4a. Some Si precipitates seem to be triangular in shape. The triangular morphology can be seen more clearly in Figure 5 when the sample was tilted to the $\langle 111 \rangle_{\alpha\text{-Al}}$ zone axis. The TEM bright-field image clearly shows that there are two different morphologies of Si precipitates: (1) the triangular-shaped Si precipitates, as marked with a white box in Figure 5a, and (2) plate-shaped Si precipitates when orientated perpendicularly to the e-beam. More interestingly, some plate-shaped Si precipitates appear to have a truncated shape, as marked with a white arrow in Figure 5a. This can be further confirmed with the dark-field image taken using the $(220)_{\text{Si}}$ diffraction spot, as marked in Figure 5c. On the basis of these observations, we propose that the triangular- and some plate-shaped Si precipitates actually have the shape of a truncated pyramid. For clarity, a schematic diagram of truncated pyramid-shaped Si precipitates is also shown in Figure 5d. Figure 5d shows the projection of the intersected $\{111\}_{\alpha\text{-Al}}$ truncated pyramid-shaped Si

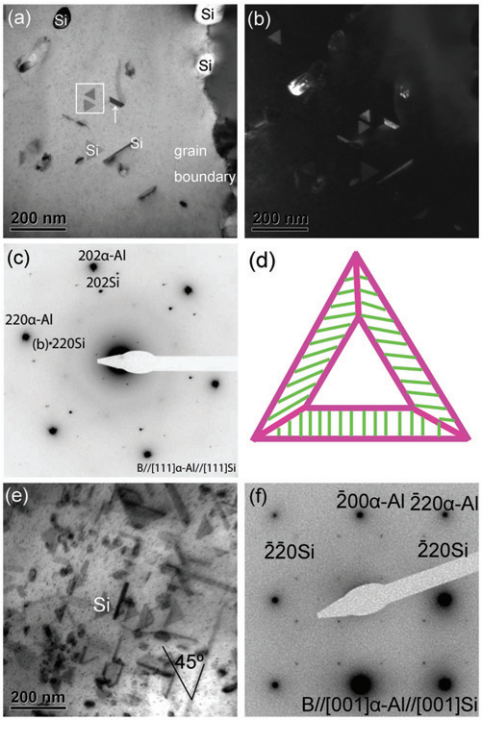

Figure 5. (a) TEM bright-field image, (b) dark-field image using the diffraction spot as marked in (c), and (c) corresponding $[111]_{\alpha\text{-Al}}$ SADP taken from melt-spun Al–5Si–50 ppm Fe–100 ppm Sr (wt%) alloy. (d) Schematic diagram showing a truncated pyramid in $\langle 111\rangle_{\alpha\text{-Al}}$ projection. The truncated $\{111\}_{\alpha\text{-Al}}$ plane are shaded, the truncated top surface is white. (e, f) TEM bright-field image and corresponding $[001]_{\alpha\text{-Al}}$ SADP, respectively.

precipitates in a $\{111\}_{\alpha\text{-Al}}$ plane of the α-Al matrix, as marked with a white box and a white arrow in Figure 5a. Viewed from another zone axis (i.e. $[001]_{\text{Si}}$, Figure 5e and f), some different projections of truncated pyramid Si precipitates were observed to have different morphologies, such as triangular or plate. However, it should be noted that plate-shaped Si precipitates, which were not observed from the truncated pyramid Si precipitates, are indeed present in the microstructure. The corresponding $\langle 111\rangle$ and $\langle 001\rangle$ SADPs (Figure 5c and f) also show that the crystallographic orientation relationship between the Si precipitates and α-Al matrix maintains a cube to cube orientation relationship, i.e. $\{111\}_{\text{Si}}\langle 110\rangle_{\text{Si}}//\{111\}_{\alpha\text{-Al}}\langle 110\rangle_{\alpha\text{-Al}}$. Similar to Figure 2b, the un-indexed diffraction points in Figures 4b and 5c and f can be also attributed to the double diffraction of Si. Owing to the double diffraction (caused by the smaller size of Si precipitates with respect to sample thickness) and the two-fold twin-reflected orientation relations (see encircled Si precipitates with a white box in Figure 5a), a complex SADP was obtained mimicking a complex cubic phase with a large unit cell as an artefact. It should be noted that the matrix around the precipitates exhibits substantial strain contrast. This is especially true for the projection where Si precipitate appears plate-shaped, and is consistent with the

precipitates in Al–Si–Ge alloy [13], where Ashby–Brown-type strain contrast [21] around rounded and fine Si–Ge precipitates was also observed. However, in contrast to the Al–Si–Ge alloy produced by arc melting and annealing, the plate-shaped and truncated pyramid-shaped precipitates are dominant in Al–Si-based alloys produced by melt spinning. This indicates that the higher cooling rate favours the formation of plate-shaped and truncated pyramid-shaped Si precipitates with clear facets.

3.2. *Controlled cooling condition*

3.2.1. *Si particles on the grain boundary in high purity melt-spun Al–5Si–50 ppm Fe–100 ppm Sr alloy after continuous controlled cooling*

After continuous controlled cooling, the size of these Si particles increases, while their number decreases in all three alloys. A few large Si particles were observed on grain boundaries. Figure 6 shows two Si particles on the grain boundary in high purity melt-spun Al–5Si–50 ppm Fe–100 ppm Sr alloy after continuous cooling in the range from 600 to 400°C with a rate of 10°C/min. Fewer twins, i.e. lower twin densities, were observed compared to the as-melt-spun condition. Viewed from different zone axes ($\langle 111\rangle_{Si}$ and $\langle 011\rangle_{Si}$), the size of the Si particles after continuous cooling was found to be about 2–3 μm in length and 1–2 μm in width. It is much larger than in as-melt-spun conditions, as shown in Figures 1a and 2a. The grain size was also estimated to increase from 0.9 ± 0.2 μm in the as-melt-spun condition to about 20 ± 2 μm after continuous cooling. It is very clear that a ripening process occurs during the continuous cooling from 600 to 400°C with a low cooling rate of 10°C/min.

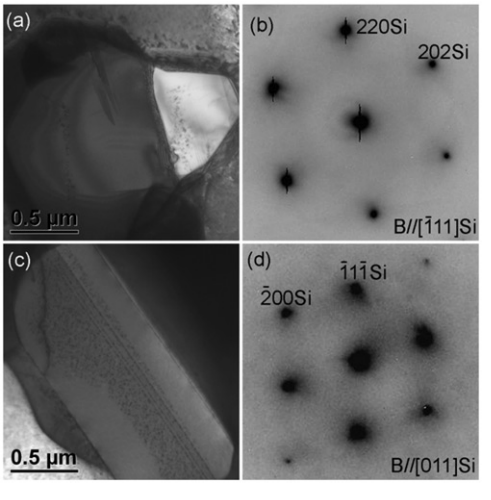

Figure 6. (a, c) TEM bright-field images, and (b, d) corresponding SADPs of the Si particles taken from Al–5Si–50 ppm Fe–100 ppm Sr (wt%) alloy after continuous cooling in the range from 600 to 400°C with a rate of 10°C/min.

3.2.2. *Si precipitates from the supersaturated solid solution in high purity melt-spun Al–5Si–50 ppm Fe–100 ppm Sr alloy after continuous controlled cooling*

After continuous controlled cooling, the Si precipitates in the α-Al matrix were observed in all three alloys. No significant differences in the morphology of Si precipitates were found among these three alloys, compared to the as-melt-spun condition, although the size of Si precipitates increases and the number density of Si precipitates decreases. Figure 7 shows a series of typical TEM images of the Si precipitates in high purity melt-spun Al–5Si–50 ppm Fe–100 ppm Sr alloy after continuous cooling in the range from 600 to 400°C with a rate of 10°C/min. Two plate-shaped Si precipitates were tilted to two different zone axes. The size of the plate-shaped Si precipitates is in the order of 500 nm in length and about 5 nm in width, with a ratio of about 100:1, as shown in Figure 7a and c. It is much larger than that in as-melt-spun condition observed in Figures 4a and 5a.

Similar to the as-melt-spun condition, some truncated pyramid Si precipitates were also observed to coexist with the plate-shaped Si precipitates after continuous cooling in the range from 600 to 400°C with a rate of 10°C/min, as marked with a white arrow in Figure 8b. The size of the truncated pyramid Si precipitates is about twice as large than that in as-melt-spun condition observed in Figure 4a. The number density of the Si precipitates was estimated to decrease from $8.5 \pm 0.4 \times 10^{20}\,\mathrm{m}^{-3}$ in the as-melt-spun condition to about $0.4 \pm 0.2 \times 10^{20}\,\mathrm{m}^{-3}$. All these results suggest that the Si precipitates grow and coarsen during controlled cooling by Oswald ripening [22]. However, the orientation relationship between these Si precipitates and the α-Al matrix still maintains cube to cube, as shown in Figures 7b, d and 8c.

The cube to cube orientation relationship can be further confirmed in Figure 9. Fast Fourier transformation taken from the α-Al matrix and the Si precipitate

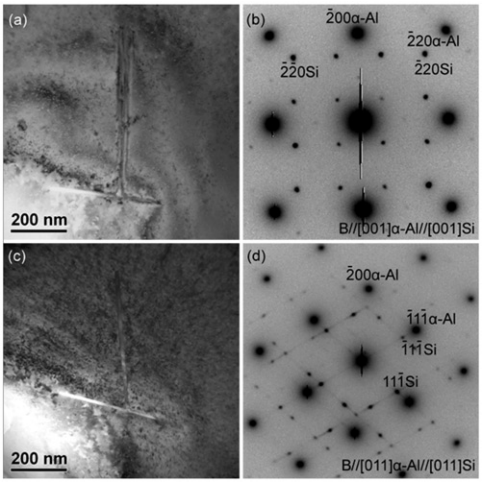

Figure 7. (a, c) TEM bright-field images, and (b, d) corresponding SADPs of the Si precipitates taken from Al–5Si–50 ppm Fe–100 ppm Sr (wt%) alloy after continuous cooling in the range from 600 to 400°C with a rate of 10°C/min.

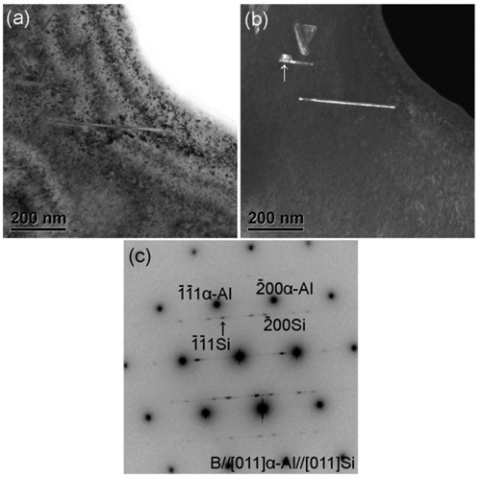

Figure 8. (a) TEM bright-field image, (b) dark-field image using the diffraction spot as marked with a black arrow in (c), and (c) corresponding $[011]_{\alpha\text{-Al}}$ SADP taken from Al–5Si–50 ppm Fe–100 ppm Sr (wt%) alloy after continuous cooling in the range from 600 to 400°C with a rate of 10°C/min.

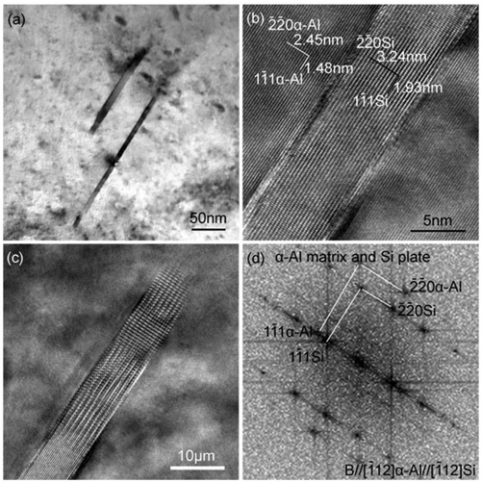

Figure 9. (a) TEM bright-field image, (b, c) high resolution TEM images, and (d) fast Fourier transformation of the α-Al matrix and the Si precipitate in Al–5Si–50 ppm Fe–100 ppm Sr (wt%) alloy after continuous cooling in the range from 600 to 400°C with a rate of 10°C/min.

(Figure 9d) indicates that the cube to cube orientation relationship between the α-Al matrix and the Si precipitates is not lost. High resolution TEM in Figure 9b shows that there is no twinning within the Si precipitates. Towards the end of the Si precipitates, the image (Figure 9c) reveals a moiré pattern, which can be attributed to overlapping of the α-Al matrix and the Si lattice. The untwinned Si precipitates

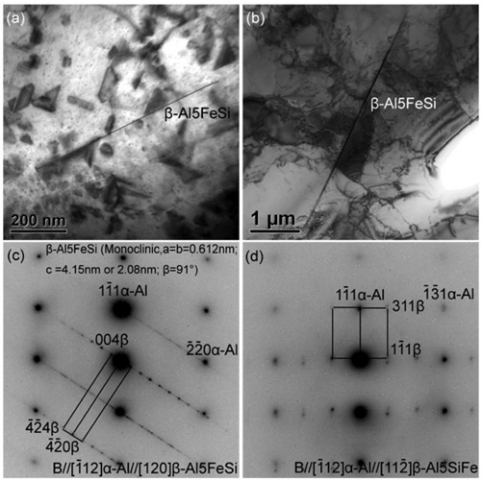

Figure 10. (a, b) TEM bright-field images, and (c, d) corresponding $[\bar{1}12]_{\alpha\text{-Al}}$ SADPs of β-Al_5FeSi in Al–5Si–200 ppm Fe (wt%) alloy after different controlled cooling. (a) Taken from the sample after continuous cooling in the range from 600 to 400°C with a rate of 10°C/min (B//$[001]_{\alpha\text{-Al}}$). (b) Taken from the sample held at 550°C for 2 h and then continuous cooled to 400°C with a rate of 200°C/min.

observed here are in contrast to the Si–Ge precipitates in Al–Si–Ge alloys [13], where the Si precipitates are all multiple twinned; the cube to cube orientation relationship between the matrix and the precipitates is also lost. This difference may be attributed to the smaller size of the Si precipitates in our study, in particular the smaller thickness (only about 5 nm) of the plate-shaped and/or truncated pyramid-shaped Si precipitates.

3.2.3. *Formation of equilibrium AlFeSi phase after continuous cooling*

Apart from the Si phase, a long platelet-like Fe-containing phase (about 700 nm in length) was also observed in Al–5Si alloy with a higher Fe content (200 ppm) after continuous cooling in the range from 600 to 400°C with a rate of 10°C/min, as shown in Figure 10a. Similarly, a Fe-containing phase (about 6.5 μm in length) was also observed in the sample after isothermal heating at 550°C for 2 h and subsequent cooling to room temperature with a rate of about 200°C/min, as shown in Figure 10b, although the latter is much larger in size than the former due to the longer holding time (2 h) at 550°C. The Fe-containing phase can be indexed as β-Al_5FeSi phase (Monoclinic, $a = 0.612$ nm; $b = 0.612$ nm; $c = 4.15$ nm; $\beta = 91°$) [23], as shown in Figure 10c and d. It should be noted that these two SADPs were taken from he different areas of the same long platelet β-Al_5FeSi phase, tilted to be the identical $\langle 112\rangle_{\alpha\text{-Al}}$ zone axis.

Another interesting observation is that the Si precipitates were connected to the β-Al_5FeSi phase after continuous slow cooling, as shown in Figure 10a. This indicated that the β-Al_5FeSi phase may influence the nucleation and growth of Si during continuous controlled cooling in the α-Al matrix. No such Si precipitates were

observed after isothermal heating and subsequent cooling, suggesting that the higher cooling rates (about 200°C/min) suppressed the precipitation of Si from the supersaturated solid solution in the α-Al matrix.

4. Discussion

4.1. *Precipitation of Si in Al–Si-based alloys*

Two types of Si particles have been observed in high purity Al–5Si-based alloy in as-melt-spun condition and after continuous controlled cooling. One is the twinned Si particles formed directly from the liquid during solidification (Figures 1–3 and 6). The other is the plate-shaped and truncated pyramid-shaped Si precipitates nucleated and grown along $\{111\}_{\alpha\text{-Al}}$ plane from supersaturated solid solution in the α-Al matrix (Figures 4, 5 and 7–9).

In terms of the twinned Si particles, the Si particles within the α-Al matrix maintain a perfect cube to cube relationship with the α-Al matrix. Furthermore, some dislocations appear to interact with the Si particle, as shown in Figure 2. This suggests that Si particles may be nucleated on some defects (i.e. dislocation and impurity) within the α-Al matrix. We believe the higher cooling rate (about 10^6 K/s) during melt spinning results into thermal strains. It is the thermal strains that create the defects with a very high density (i.e. point defect substituted atoms and quenched-in excess vacancies) and line defect (dislocation)). In fact, very often, the dislocation was observed in melt spun Al–Si-based alloys (not especially shown in present paper). The kinetics of Si precipitation is affected by these defects in both liquid-quenched (rapidly solidified) and solid-quenched (quenched after annealing the solid at elevated temperature) alloys. On the other hand, the stress can be also caused by the precipitation of Si in the solidifying Al matrix. However, the stress caused by the precipitation of Si may be negligible to the formation of the defects, when compared to the thermal strains caused by melt spinning. This suggestion is consistent with a previous paper [24], where the same interfacial energy per mole Si in the precipitate ($E_{Si/Al}$) were obtained though two different experiments (TEM and DSC), although a possible contribution of elastic energy due to misfit of Si particles in the Al matrix to the enthalpy would influence the determination from the DSC data, whist it would not influence the determination from the TEM data, indicating that elastic energy is negligible.

In terms of Si precipitates within the α-Al matrix, two different morphologies of these Si precipitates were observed. One is plate-like (Figures 4, 7 and 9). The other is truncated pyramids (Figures 5 and 8). It is generally accepted that the morphology of the growing Si depends on the growth mode [25]. The growth mode can be related to undercooling. A low undercooling (less than 100°C) leads to a thin plate morphology of Si precipitates, showing a typical feature of lateral growth. A high undercoolings (greater than 210°C) leads to a randomly distributed dendrite morphology, showing a typical feature of continuous growth. In the range from 100 to 210°C, the morphology of Si shows not only a feature of lateral growth, but also a feature of continuous growth, indicating that Si grows in an intermediate mode. In our previous report [20], the addition of 50 ppm Sr into Al–5Si alloy increased the eutectic nucleation undercooling from 31 to 49°C. In this study, the addition of

100 ppm Sr also increased the undercooling (about 55°C, less than 100°C, measured from DSC, not shown here). This can partly explain why most of Si precipitates are plate-like in as-melt-spun condition, although truncated pyramidal Si precipitates were observed.

In terms of the truncated pyramidal Si precipitates, the triangular projection, as marked with a white box in Figure 5a, is shown to be aligned with a $[111]_{\alpha\text{-Al}}$ zone axis; thus, the triangular form appears to reflect the inverse three-fold symmetry of Si precipitates. This alignment gives the triangular faces as $\{111\}_{Si}$ planes, suggesting that these $\{111\}_{Si}$ planes have the lowest interfacial energy with the Al matrix. This suggestion is fully consistent with the calculated crystal-melt interfacial energy (γ) using the empirical Stillinger–Weber potential [26], where γ_{001}, γ_{111} and γ_{011} have been reported to be 0.42 ± 0.02, 0.34 ± 0.02 and $0.35 \pm 0.03\,J/m^2$, respectively. The calculated γ is also in a reasonable agreement with the reported experimental results γ_{111} (0.34–0.45 J/m^2) obtained based on the classical theory of nucleation [27,28]. Clearly, the crystal-melt interfacial energy of γ_{111} is substantially smaller than that of γ_{001}, although nearly identical to that of γ_{011}. This is consistent with the observation in Figure 9, where the Si precipitate grows along the $\{111\}_{Si}$ planes, and the observation in Figures 3 and 4, where the Si twinning occurs along the $\{111\}_{Si}$ planes. This qualitative trend in anisotropy (γ) can also partly explain why truncated pyramids Si precipitates nucleate and grow along $\{111\}_{\alpha\text{-Al}}$ plane, as marked with a white arrow in Figure 5a.

The nucleation and growth of Si precipitates is also influenced by surface free energy. In a supercooled liquid, interfacial energy (γ) serves to counteract the effect of surface free energy difference between solid and liquid phases. A lower γ means that more driving force (undercooling) is required for the nucleation and growth of Si. The surface free energies of {001} and {110} planes have been reported to be 1.09 ± 0.07 and 1.07 ± 0.03 times that of {111} planes, respectively [29]. The lower surface free energy of Si {111} compared with other orientations (i.e. Si {001}, Si {011}) results in higher undercooling. To lower the surface free energy, the equilibrium Si {001} melt interface develops {111} facets, thus resulting a rough interface. On the other hand, Si {111} melt interface remains smooth and sharp (flat) due to its higher stability (as seen in Figure 3). Thus, from simple geometrical considerations, the truncated pyramid can be formed by slicing parallel to a {111} face, to chop off the corner of a cube made of {100} facets, so forming a pyramid, and then chopping off the top of this pyramid by again slicing parallel to a {111} face. This produces a truncated pyramid with lower and upper {111} faces. The original {100} facets of the cube form the other three, inclined faces that are portrayed with green dashes in Figure 5d. This suggestion is also consistent with the previous report [30], where a rounded Si surface was seen about the [001] direction of all cavities formed by ion implanting $\{001\}_{Si,}$ and the most frequently observed facets are {111} planes, although {110} facets were seen less frequently. It should be noted that the argument about the influence of interfacial energy on the formation of the truncated pyramids of Si is framed in terms of a supercooled liquid [25] and equilibrium Si melt [26]. However, we believe there is no big difference on the interfacial energy and the growth mode of Si precipitates between the liquid–solid transformation (solidification from liquid, i.e. melt spinning) and solid–solid transformation (precipitation from the supersaturated solid solution). Liquid–solid

transformation can be attributed to the precipitation of dissolved Si and coarsening of Si particles already present in the as-liquid quenched state, whereas solid–solid transformation can be ascribed solely to precipitation of Si. Although the required driving force may be different (in the case of liquid–solid transformation, the driving force is undercooling, while, in the case of solid–solid transformation, the driving force is supersaturated solid solution), it does make sense to discus the interfacial energy and the growth mode in a similar manner. For example, in the case of solid–solid transformation, the Si precipitates nucleate and grow along the $\{111\}_{Si}$ planes (Figure 5), while, in the case of liquid–solid transformation, the Si twinning also occurs along the $\{111\}_{Si}$ planes (Figure 3), just due to the fact that the crystal-melt interfacial energy of γ_{111} is smaller than that of γ_{001}, although nearly identical to that of γ_{011} [26].

4.2. *The influence of Sr and Fe addition*

A twinned Si particle was observed in high purity melt spun Al–5Si alloy without any addition of Sr and Fe, as shown in Figure 1a. The formation of the twinned Si particle can be attributed to the higher quenching rate during melt spinning. However, it also suggests that Si twinning may be a natural process during nucleation and growth of Si and independent on the impurity because the Al–5Si alloy does not contain modifying elements (i.e. Na, Sr, etc.), even at a very low level. This suggestion is consistent with the previous report on quenching modification [17].

The addition of 100 ppm Sr in Al–5Si-based alloy leads to a heavily multiply twinned Si particle, as shown in Figure 3. According to the well-known IIT [17] and TPRE [18,19], Sr is proposed to be adsorbed on the growing surfaces of Si and cause frequent twinning to occur. Both IIT and TPRE mechanism have been experimentally supported in case of Sr [14–16]. Sr has been observed to be present in the eutectic Si of Al–Si-based alloys using μ-XRF mapping [14], atom probe tomography (APT) [15] and electron probe microanalysis technique (EPMA), respectively, although μ-XRF mapping and EPMA reveal that Sr is homogenously distributed within the eutectic Si, while APT shows Sr is segregated at the Al/Si eutectic interface on the side of the eutectic Al region. This difference may be due to the techniques and resolution used. The heavily multiply twinned Si particles (Figure 3) observed here can also provide strong experimental evidences to the IIT and TPRE mechanism. Further research to detect single Sr atoms along the Si twinning is in progress and will be reported elsewhere.

The addition of up to 200 ppm Fe does not greatly change the Si twinning and the precipitation of Si. No Si precipitates were observed within the α-Al matrix. Furthermore, no Fe-containing phase was observed in melt-spun Al–5Si–200 ppm Fe alloy. The β-Al_5FeSi phase was only observed after heat treatment to obtain equilibrium, i.e. after continuous cooling in the range from 600 to 400°C with a rate of 10°C/min (Figure 10a) or after isothermal heating at 550°C for 2 h and subsequent cooling to room temperature with a rate of about 200°C/min (Figure 10b). This strongly indicates that higher cooling rates suppress the formation of β-Al_5FeSi phase. This is in a good agreement with the case of commercial casting

(i.e. high pressure die casting), where α-AlFeSi phase, instead of β-Al_5FeSi phase, is dominant due to the higher cooling rates. Furthermore, the larger size of β-Al_5FeSi phase shown in Figure 10b, compared to Figure 10a, indicates that the β-Al_5FeSi phase may form, survive and grow during the isothermal heating at 550°C for 2 h. The absence of Si particles in the vicinity of larger β-Al_5FeSi phase (Figure 10b) also indicates that the higher cooling rate (about 200°C/min) can effectively suppress the precipitation of Si within the α-Al matrix in case of Al–5Si–200 ppm Fe alloy. This is also consistent with the absence of Si precipitates in as-melt-spun Al–5Si-200 ppm Fe alloy. However, it is in contrast to the case of Al–5Si–50 ppm Fe–100 ppm Sr alloy, where the addition of 100 ppm Sr into Al–5Si alloy promotes the precipitation of Si in the supersaturated α-Al matrix, even in as-melt-spun condition. The enhanced precipitation of Si caused by the addition of 100 ppm Sr can be attributed to the decrease in Si solubility in the α-Al matrix and the possible formation of Sr_3P_2 compounds (as discussed later), although the content of Fe (50 ppm) is lower than that (200 ppm) in Al–5Si–200 ppm Fe alloy.

As regards nucleation, the addition of Sr is believed to have a negative effect on the potency of AlP phase due to the possible formation of the Sr_3P_2 phase. It is well known that AlP (not detected here) phase is a potent nucleation site for eutectic Si. The possible formation of the Sr_3P_2 phase results into smaller quantities of P available in the melt to form AlP, thus a larger undercooling can be achieved. The larger undercooling (more driving force) promotes the nucleation and growth of Si. This can partly explain why the Si precipitates were only observed in as-melt-spun Al–5Si–50 ppm Fe–100 ppm Sr alloy. However, it is worth noting that all the materials in this study are based on the high purity. The content of P can be expected to be at a very low level (less than 2 ppm, as reported in [20]). It is, thus, reasonable to expect that the effect, caused by the formation of Sr_3P_2 phase, on nucleation of Si was not significant. Instead, it is the segregation of Sr into Si [14–16] that hinders the TPRE growth of Si and hence stimulates the isotropic growth of Si, which results in an increasing twinning frequency, a multiply Si twinning (Figure 3) and finally a fine fibrous morphology. The stimulated isotropic growth of Si can also partly explain why the addition of Sr results into some Si precipitates present to be truncated pyramids, rather than flatter plates.

The addition of Sr can also result into the formation of Al_2Si_2Sr phase [20] at lower Sr level (i.e. 100 ppm in this study) and Al_4Sr phase at very high Sr level (i.e. 3000 ppm). However, it is highly unlikely that these intermetallics act as nuclei for Si due to the high disregistry between Si and these intermetallic particles. Considering that P is consumed by the formation of Sr_3P_2 compounds, then a question arises, how to nucleate the eutectic Si at a larger undercooling? Given the unique solidification conditions during melt spinning and the use of high purity materials for alloy preparation, the β-Al_5FeSi phase is believed to be a nucleation site for eutectic Si in hypoeutectic Al–Si alloys in the absence of AlP. This is consistent with the fact that some silicon particles appear to have nucleated on a large plate-like β-Al_5FeSi phase (Figure 10a), although no strong respective high symmetry with crystallographic orientation relationship was observed. However, it should be pointed out that the nucleation potency of β-Al_5FeSi phase also depends upon the material processing conditions. In normal sand/or permanent mould casting, where the cooling rates are relatively slow, β-Al_5FeSi is large in size and plate-like

in morphology. Generally, it can not act as a nucleus for Si. However, in as-melt-spun condition, β-Al_5FeSi is greatly refined, and can act as a substrate for Si nucleation.

5. Conclusion

Two types of Si particles have been investigated in high purity Al–5Si-based alloys in as-melt-spun condition and after continuous controlled cooling. One is the twinned Si particles formed directly from the liquid during solidification. The other is the plate-shaped and truncated pyramid-shaped Si precipitates nucleated and grown along $\{111\}_{\alpha\text{-Al}}$ plane from supersaturated solid solution in the α-Al matrix. The addition of Sr into Al–5Si-based alloys was found to promote the formation of the Si precipitates in the supersaturated α-Al matrix and twinning of the Si particles on the grain boundary from the liquid state. The β-Al_5FeSi phase was only observed after heat treatments to obtain equilibrium. The β-Al_5FeSi phase can be also a nucleation site for eutectic Si in Al–5Si-based alloys in the absence of AlP. This microstructure characterisation provides a better understanding of the nucleation and growth of Si in high purity melt spun Al–Si-based alloys.

Acknowledgements

JL gratefully acknowledges Gabriele Moser and Dr Boriana Rashkova for their help with TEM sample preparation at the Erich Schmid Institute of Materials Science of the Austrian Academy of Science. MZZ acknowledges financial support from the Higher Education Commission (HEC) of Pakistan and cooperation from the OEAD.

References

[1] M. Makhlouf and H.V. Guthy, J. Light Metals 1 (2001) p.199.
[2] A.K. Dahle, K. Nogita, S.D. McDonald, J.W. Zindel and L.M. Hogan, Metall. Mater. Trans. A 32 (2001) p.949.
[3] A.K. Dahle, K. Nogita, S.D. McDonald, C. Minnis and L. Lu, Mater. Sci. Eng. A 413–414 (2005) p.243.
[4] Y.H. Cho, H.-C. Lee, K.H. Oh and A.K. Dahle, Metall. Mater. Trans. A 39 (2008) p.2435.
[5] N.L. Tawfik, J. Mater. Sci. 32 (1997) p.2997.
[6] O. Uzun, F. Yılmaz, U. Kölemen and N. Başman, J. Alloys Compd. 509 (2011) p.21.
[7] O. Uzun, T. Karaaslan, M. Gogebakan and M. Keskin, J. Alloys Compd. 376 (2004) p.149.
[8] C. Triveño Rios, M.M. Peres, C. Bolfarini, W.J. Botta and C.S. Kiminami, J. Alloys Compd. 495 (2010) p.386.
[9] Y. Birol, J. Alloys Compd. 439 (2007) p.81.
[10] N. Ünlü, A. Genç, M.L. Öveçoğlu, E.J. Lavernia and F.H. Froes, J. Alloys Compd. 343 (2002) p.223.
[11] N. Ünlü, A. Genç, M.L. Öveçoğlu, N. Eruslu and F.H. Froes, J. Alloys Compd. 322 (2001) p.249.

[12] C.L. Xu, H.Y. Wang, F. Qiu, Y.F. Yang and Q.C. Jiang, Mater. Sci. Eng. A 417 (2006) p.275.
[13] D. Mitlin, U. Dahmen, V. Radmilovic and J.W. Morris Jr, Mater. Sci. Eng. A 301 (2001) p.231.
[14] K. Nogita, H. Yasuda, K. Yoshida, K. Uesugi, A. Takeuchi, Y. Suzuki and A.K. Dahle, Scripta Mater. 55 (2006) p.787.
[15] M. Timpel, N. Wanderka, G.S. Vinod Kumar and J. Banhart, Ultramicroscopy 111 (2011) p.695.
[16] M. Faraji and L. Katgerman, Micron 41 (2010) p.554.
[17] S.Z. Lu and A. Hellawell, Metall. Mater. Trans. A 18 (1987) p.1721.
[18] R.S. Wanger, Acta Metall. 8 (1960) p.57.
[19] R.D. Hamilton and R.G. Seidensticker, J. Appl. Phys. 31 (1960) p.1165.
[20] M. Zarif, B. McKay and P. Schumacher, Metall. Mater. Trans. A 42 (2011) p.1684.
[21] M.F. Ashby and L.M. Brown, Philos. Mag. 8 (1963) p.1083.
[22] I.M. Lifshitz and V.V. Sylozov, J. Phys. Chem. Solids 19 (1961) p.35.
[23] G. Sha, K.A.Q. O'Reilly, B. Cantor, J. Worth and R. Hamerton, Mater. Sci. Eng. A 304–306 (2001) p.612.
[24] M.J. Starink and A.-M. Zahra, Philos. Mag. A 77 (1998) p.187.
[25] Z.Y. Jian, K. Kuribayashi, W.Q. Jie and F.G. Chang, Acta Mater. 54 (2006) p.3227.
[26] P.A. Apte and X.C. Zeng, Appl. Phys. Lett. 92 (2008) p.221903.
[27] M. Gündüz and J.D. Hunt, Acta Metall. 37 (1988) p.1839.
[28] S.R. Stiffler, M.O. Thompson and P.S. Peercy, Phys. Rev. Lett. 60 (1988) p.002519.
[29] D.M. Follstaedt, Appl. Phys. Lett. 62 (1993) p.1116.
[30] S. Somasi and B. Khomami, J. Phys. Chem. B 108 (2004) p.19721.